Physical models, cross sections, and numerical approximations used in MCNP and GEANT4 Monte Carlo codes for photon and electron absorbed fraction calculation

Hélio Yoriyaz,[a] Maurício Moralles, Paulo de Tarso Dalledone Siqueira, Carla da Costa Guimarães, Felipe Belonsi Cintra, and Adimir dos Santos
Instituto de Pesquisas Energéticas e Nucleares, IPEN-CNEN/SP, São Paulo 05508–000, Brazil

(Received 9 April 2009; revised 3 September 2009; accepted for publication 4 September 2009; published 13 October 2009)

Purpose: Radiopharmaceutical applications in nuclear medicine require a detailed dosimetry estimate of the radiation energy delivered to the human tissues. Over the past years, several publications addressed the problem of internal dose estimate in volumes of several sizes considering photon and electron sources. Most of them used Monte Carlo radiation transport codes. Despite the widespread use of these codes due to the variety of resources and potentials they offered to carry out dose calculations, several aspects like physical models, cross sections, and numerical approximations used in the simulations still remain an object of study. Accurate dose estimate depends on the correct selection of a set of simulation options that should be carefully chosen. This article presents an analysis of several simulation options provided by two of the most used codes worldwide: MCNP and GEANT4.
Methods: For this purpose, comparisons of absorbed fraction estimates obtained with different physical models, cross sections, and numerical approximations are presented for spheres of several sizes and composed as five different biological tissues.
Results: Considerable discrepancies have been found in some cases not only between the different codes but also between different cross sections and algorithms in the same code. Maximum differences found between the two codes are 5.0% and 10%, respectively, for photons and electrons.
Conclusion: Even for simple problems as spheres and uniform radiation sources, the set of parameters chosen by any Monte Carlo code significantly affects the final results of a simulation, demonstrating the importance of the correct choice of parameters in the simulation. [DOI: 10.1118/1.3242304]

Key words: dosimetry, Monte Carlo, absorbed fraction, MCNP, GEANT4

I. INTRODUCTION

The Monte Carlo method to simulate radiation transport has become the most common means of calculating particle flux or energy deposition distribution and other quantities of interest in several areas of nuclear engineering and medical physics. In this last area, the application of Monte Carlo techniques covers many segments like radiotherapy, diagnostic radiology, radiation protection, and nuclear medicine. Nowadays, with the increasing progress in the computer technology, treatment planning for external beam therapy based on Monte Carlo algorithm is already commercially available for clinical use.[1]

Specifically in nuclear medicine, it is very important to accurately evaluate the absorbed fractions (AFs) in target structures or tissues due to the administration of radioactive medicines. It is basically performed by estimating the energy deposition in these target regions. This concept was first introduced by Loevinger and Berman[2] as a first pamphlet of the Medical Internal Radiation Dose Committee—MIRD publications. The formalism created in this work has been generally accepted and used since then for the majority of the scientific community in this area. Berger[3] provided the energy deposition in water by photons isotropically emitted from point sources in spheres of various sizes. These evaluations were published in MIRD Pamphlet No. 2, which also contains a tabulation of build-up factors and related data for energy deposition in water. Nineteen monoenergetic photon sources were considered with energies ranging from 0.015 to 3 MeV.

Brownell *et al.*[4] evaluated the absorbed fractions for photon dosimetry in tissue-equivalent materials. In this work, the absorbed fractions were assessed in spheres and cylinders from 2 to 200 kg and ellipsoids from 0.3 to 6 kg for photon energies in the 0.02–2.75 MeV range. This was further published in MIRD Pamphlet No. 3.

Akabani *et al.*[5] estimated beta absorbed fractions in small localized tumors represented by spheres of different sizes, with radius varying from 0.1 to 2.0 cm. The beta sources were uniformly distributed within the spheres considering the average energy of the beta spectra to be representative of the radionuclide. Monoenergetic electron sources with ener-

gies from 0.05 to 4 MeV were therefore considered. Cut-off energies were set as 10 keV for electrons and 1 keV for photons. The calculations were performed using the Monte Carlo code EGS4—Electron Gamma Shower[6] for electron and photon transport in tissue-equivalent elemental composition media which was based on the data given by MIRD Pamphlet No. 5.[7]

Siegel and Stabin[8] also evaluated the absorbed fractions for electron and beta sources uniformly distributed within spheres of various sizes using the methodology developed by Berger. Energies varied from 0.062 to 1.428 MeV and from 0.025 to 4 MeV, respectively, for beta and electron sources. Afterward, Stabin and Konijnenberg[9] re-evaluated those values using two different Monte Carlo codes, EGS4 and MCNP-4B,[10] showing some interesting discrepancies between the results. In some cases, these discrepancies exceeded 10% of the obtained values. This work also presented recommended values which were estimated as the average results of the two codes. The important issue raised from this work is the considerable discrepancies that can be found when different Monte Carlo codes are used, demonstrating the complexity of dose evaluation task which involves several factors as cross sections, numerical approximations, and physical models.

The objective of the present work is to better evaluate the discrepancies in the calculation of the absorbed fractions for photon and electron sources in spheres of some biologically interesting materials using different codes. The focus is on the use of MCNP-4C,[11] MCNP5,[12] and GEANT4 (Ref. 13) Monte Carlo codes, which nowadays are among the most used codes worldwide. For the evaluation of the discrepancies, many of the absorbed fractions values published are reproduced here. Investigations have also been conducted in an attempt to recognize the main causes of those discrepancies not only between the codes but also discrepancies generated when using different models, cross sections, and numerical approximations in the same code. Finally, after the definition of the most suitable set of parameters for simulation in MCNP and GEANT4, the averaged electron and photon absorbed fractions in spheres of several sizes and composed of five different biological tissues are presented.

II. MATERIAL AND METHODS

Although the MCNP and GEANT4 codes have been used in medical physics for some time, they were originally conceived to simulate experiments of nuclear and particle physics, respectively, and are the result of many decades of development. The differences and uniqueness in their primary aims and in their development processes turned them to eventually have distinct simulating/tallying procedures which bestowed them particular characteristics. This section intends to present a glance on some of these simulating characteristics which were evaluated to play a relevant role on the studied parameters (photon and electron source absorbed fractions).

In all simulations the energy cut-off was set to 2.93 keV for photons and 9.4 keV for electrons and the statistical errors were less than 0.5%. The basis for the selection of quoted energy cutoffs is (a) the electron range in water, with the quoted energy of 9.4 keV, is approximately 0.002 mm, which is far smaller than 10% of the smallest sphere radius (0.065 mm). Such set follows the MCNP manual recommendation concerning the minimum number of electron steps in the target volume (b) The mean free path of photons of quoted energy of 2.93 keV is 1 mm, which is less than 10% of the smallest sphere diameter (12.4 mm).

II.A. The MCNP code

The MCNP code is used worldwide to solve neutron, photon, and electron coupled transport problems. Its main features are the versatile and powerful general source characterization, flexible tally features, and variance reduction schemes. Photon interaction models include photoelectric effect, pair production, incoherent scattering, and coherent scattering including the form factors to account for electron binding effects. By default the photon cut-off energy is 1 keV. The photon cross sections are based on ENDF evaluated data.[14]

The most important theories for electron transport algorithm in MCNP are the Goudsmit–Saunderson for angular deflections and Landau theory with its enhanced version by Blunck and Leisegang for energy straggling due to collisions.[11] Basically, the electron transport algorithm structure is composed of a sequence of energy steps which characterize the condensed random walk firstly introduced by Berger.[15] As a very versatile radiation transport code, MCNP provides a wide set of possibilities to tail the simulation according to the user needs. However, the proper use of such potentiality requires the access and assignment of adequate input parameters by the user. Three of the most important issues affecting the absorbed dose estimates are briefly presented below, as these points have already been studied and pointed out before.[16–22]

II.B. Scoring tally in MCNP

MCNP provides an assorted set of ways to estimate dose/energy deposition for typical simulation runs. Two of the most straightforward dose/energy deposition evaluation ways are assessed by F6 and *F8 tallies. The track length estimator for energy deposition—F6 tally—is a photon track length flux estimator modified by the convolution with energy-dependent mass energy absorption coefficients. It assumes that all energies transferred to electron are deposited locally and therefore is a KERMA based tally. *F8 tally in turn, is a tally pulse height. Whenever a particle goes from one region to another, the amount of energy it carries is subtracted from

the account of the exiting region and is added to the region where the particle enters. This tally is used for both photons and electrons.

An alternative option to access dose/energy deposition is by using the track length estimator, F4, which works equally for neutron, photon, and electron. Such procedure, however, demands coupling extra tally cards to the input deck. One can reproduce F6 outcomes with F4 just by coupling a specific FM card and turning off secondary electron transport.[11] In order to estimate dose delivered by electrons, one must present a pointwise flux-to-dose conversion data set by the DE/DF cards together with the F4 tally.

Version 5 of the code also provides another F4-based dose estimation in combination with DF/DE function by means of FMESH card which allows superimposing a mesh tally over the geometry, avoiding the so-called boundary crossing artifacts. The version used in this work allows two types of virtual surface geometry: Rectangular or cylindrical, so cylindrical geometry was adopted for dose estimation in the range of energy and size considered in the present work. Sec. III A shows the comparison of energy deposition values obtained using F6- (KERMA), *F8-, and F4-based tallies.

II.C. Energy indexing algorithm

There are two options for the interpolation procedure necessary for the determination of energy loss rate and multiple scattering angles which are based on different energy binning techniques: default and ITS modes. Schaart *et al.*[18] and Reynaert *et al.*,[20] among others, demonstrated the discrepancies found between these two techniques using the version 4C. In this work the investigation of those discrepancies is evaluated with version 5 for internal sources involving spheres of various sizes. The results and discussion are presented in Sec. III B.

II.D. Transport parameters

A brief analysis of differences in the MCNP energy deposition values caused by the change in the electron cross section library (EL1 and EL03) demonstrated no significant discrepancies in the results. On the other hand, a change in the photon cross-section library causes some significant discrepancies in dose estimates. The MCNP photon libraries are based on the EPDL dataset and it is already a known fact that for low photon energies dose values obtained with photon cross-section libraries distributed with the version 4C (MCPLIB01) introduce an underestimation in dose rate in water of about 7.8% compared to the XCOM library.[23] This problem was overcome with the new library (MCPLIB04) distributed together with the version 5. This library was introduced in 2002 and was processed from the ENDF/B-VI.8,[24] which, in turn, based its photoatomic and atomic relaxation data on the EPDL97 (Ref. 25) library, which does not include *L*-shell fluorescence. In the present work, the dose differences have been quantified specifically for internal sources in spheres of various sizes and for several source energies.

Four photon libraries delivered with the distribution have been tested: MCPLIB, MCPLIB02, MCPLIB03, and MCPLIB04. Section III C shows the discrepancies found when using different libraries.

II.E. The GEANT4 code

GEANT4 is a radiation transport simulation package that allows calculating the continuous or discrete energy loss during the passage of radiation through matter. The electron transport in GEANT4 is performed with a class II condensed history algorithm. It employs a multiple scattering algorithm based on the Lewis theory,[26] which gives information about the moment, the angular, and the spatial displacement of the particles to provide more precise simulation. To compute energy loss, a range cutoff is set, a parameter which controls both particle step length and the secondary particle production. For each material, the range cutoff of each particle is converted into an energy cutoff. Energy loss is accounted through two distinct procedures: Below a preselected energy threshold, the energy loss is assumed as a continuous process, while above it, the energy loss is due the secondary particle production. In GEANT4 all primary and secondary particles are tracked down to zero energy by default.

GEANT4 also presents three electromagnetic physics models—standard, low energy and Penelope—at the user's choice to perform electron/photon transport. The main characteristics of each electromagnetic physics models available are presented in the sequence. The accuracy of GEANT4 concerning electron and photon physics has been investigated by several groups, and detailed differences among these physical models are discussed in literature.[26–28]

II.F. Standard model

In the GEANT4 standard package, physical processes are valid for gammas and electrons from 1 keV to 100 TeV. Transport of x and gamma rays takes into account Compton scattering using the free-electron approximation, gamma conversion into electron-positron pair, and photoelectric effect. Bremsstrahlung and ionization are the available processes for electrons (Möller scattering) and positrons (Bhabha scattering). In this package the physical processes are based on theoretical corrected cross sections. An analytical approach combines numerical databases with analytical cross-section models assuming quasifree atomic electrons, while the atomic nucleus is fixed.[26] For this package, Rayleigh scattering and atomic relaxation processes are not included.

II.G. Low-energy model

The implementation of the low-energy package is valid for energies down to 250 eV. The available physical processes are Rayleigh scattering, Compton scattering, photoelectric effect, gamma conversion (pair production), bremsstrahlung, and ionization. The fluorescence of and Auger emission in excited atoms are also considered. This package describes the electromagnetic interactions of electrons and

TABLE I. Photon energy deposition percentage differences in water spheres between MCNP F6 and *F8 tallies. Reference: *F8.

Sphere mass (g)	Photon source energy (MeV)		
	0.01	0.1	1
1	0.1	0.8	18.2
10	0.1	0.1	6.6
100	0.1	0.2	3.5
1000	0.1	0.2	1.6

TABLE II. Electron energy deposition percentage differences in water spheres due to different energy indexing algorithms. Reference: ITS.

Sphere mass (g)	Electron source energy (MeV)			
	0.1	1	2	4
1	0.0	0.0	−6.6	−6.1
10	0.0	0.0	0.0	−6.0
100	0.0	0.0	0.0	−0.1
1000	0.0	0.0	0.0	−0.1

photons taking into account detailed features, such as subshell integrated cross sections for photoelectric effect, ionization, and electron binding energies for all subshells. The low-energy model employs the evaluated data libraries from Lawrence Livermore National Laboratory, EPDL97 (Ref. 25) for photons, EEDL (Ref. 29) for electrons, and EADL (Ref. 30) for fluorescence and Auger effects. In this model, all atomic shells are included in the atomic relaxation processes.

II.H. Penelope model

The Penelope package is an alternative to the low-energy package. It summarizes the physical interaction processes related to photons and electrons with energies ranging from a few hundred eV to ~1 GeV of the computer code system PENELOPE (Penetration and Energy Loss of Positrons and Electrons).[31] In this package, bremsstrahlung emission is simulated using partial-wave data instead of analytical approximate formulas, and elastic and inelastic scattering are mixed for electron and positron particles. Rayleigh scattering, photoelectric effect—which considers absorption in *K* and *L* shells, described from the corresponding partial cross sections—and fluorescence radiation from vacancies in *K* and *L* shells, gamma conversion, and Compton scattering are used for photons. Section III E presents the comparison of results obtained from different physical models in GEANT4.

II.I. Specific choices for the simulation parameters

The absorbed fraction determination in spheres of various sizes has been done under a specific set of simulation parameters. This set was defined through simulations of 1, 10, 100, and 1000 g water spheres irradiated either by several monoenergetic photon or electron sources were performed. Simulation parameters consist of source definition, cut-off settings for secondary particle production, energy indexing algorithm determination, energy deposition scoring procedures, and transport parameter data. Point isotropic source was placed at the center of the sphere which was immersed in a 50 cm high and 50 cm diameter water cylinder.

The comparison between different parameters is presented as percentage relative difference calculated by

$$\text{Difference}\ (\%) = \left[\frac{(R_0' - R_0)}{R_0} \cdot 100\right], \quad (1)$$

where R_0 is the reference deposited energy and R_0' corresponds to the value to be compared.

III. RESULTS AND DISCUSSIONS

III.A. Comparison of scoring functions in MCNP

In order to evaluate and confront different energy deposition tallies provided by MCNP, F6-, *F8-, and F4-based tallies, a set of simulations was performed. Table I shows the difference in percentage, calculated with Eq. (1), considering photon sources of 0.01, 0.1, and 1 MeV. As aforementioned, energy deposition estimated by F4 tally retrieves equivalent values to those obtained by F6 tally, and therefore has been omitted from Table I. For energies of 0.1 MeV and below, no significant discrepancies were found, but it becomes relevant as the source energy increases, becoming even worse for small volumes. Results obtained using F6 are systematically greater than those obtained by *F8 tally, which for comparison purpose were adopted as the reference values. In the worst case, F6 tally overestimates the dose by about 18.20%

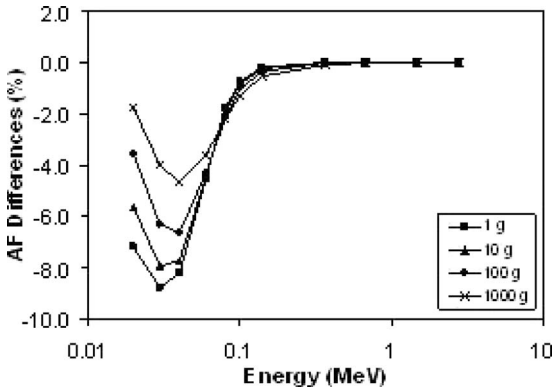

FIG. 1. Percentage differences in the absorbed fractions in water spheres of various sizes using different cross section libraries: MCNP4C/MCPLIB03 and MCNP5/MCPLIB04. Reference: MCNP5/MCPLIB04.

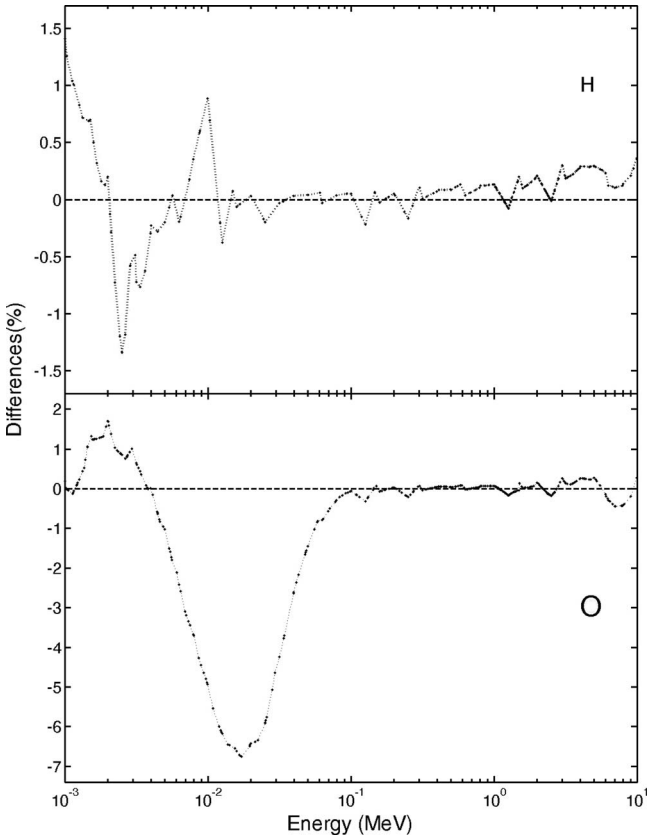

FIG. 2. Total photon cross-section differences between MCPLIB03 and MCPLIB04 for (a) hydrogen and (b) oxygen. Reference: MCPLIB04.

(1 g water sphere at 1 MeV photons). This is explained because in the track length energy deposition estimator (F6) all photon lost energies are transferred to the medium in the site of interaction. This is equivalent to the situation where all the secondary electrons are absorbed locally. In fact, no electron transport is taken into account for tally purposes. For large volumes and low energies, this aspect diminishes its influence on the energy deposition estimates because most of the electrons remain within the volume. On the other hand, for small volumes and high energies, this aspect becomes relevant.

Simulations performed to evaluate differences in electron energy deposition tally procedure were also carried out. Dose estimation using electron track length modified by DE/DF function gave no significant differences compared to *F8 dose estimates in the range of source energy of 0.1–4 MeV and target mass range of 1–1000 g. On the other hand, the utilization of FMESH virtual surfaces provided dose values 2%–11% greater, depending on the source energy and target mass considered. The differences found above is a quantification of dose error introduced by different tallying methodologies.

Since the simulations in this work present fairly simple geometry, not involving the necessity of an extensive region segmentation and due to the fact that for single surface problems *F8 tally dose estimation agreed very well with F4/DF/DE estimative, we adopted *F8 tally option in further simulations since it is the most straightforward form to compute energy deposition.

III.B. Electron energy indexing algorithm in MCNP

Likewise the procedure presented in Sec. III A, energy deposition in water spheres of various sizes was estimated using tally *F8 considering both the standard and ITS modes for electron energy indexing algorithm. Point isotropic monoenergetic electron sources with energies of 0.1, 1, 2, and 4 MeV were considered. Percentage differences between the two modes are shown in Table II. As can be observed, standard indexing algorithm (SIA) gives systematically smaller values than ITS indexing algorithm (ITA)—the adopted reference values. In the same way, differences become more relevant for small volumes and high energies. This is consistent with the results presented by Reynaert *et al.*[20] and Schaart *et al.*[18] for monoenergetic pencil beam depth dose distributions in water phantoms where the region of maximum dose build-up provided by SIA is shifted more deeply into the phantom than that provided by ITA. Similarly, in the present case, electrons deposit more energy in longer distances from the source with SIA than with ITA. Both cases are explained by the differences in the indexing algorithm parameter.

The SIA assigns the transport parameters (scattering cross sections) from the energy step that the electron energy lies on. On the other hand, the ITA mode assigns the transport parameters from the energy step whose upper boundary is closest to the electron energy. Since the scattering cross sections are calculated for the upper boundary of the energy step, cross sections obtained by SIA correspond to an energy half group higher in the energy grid. As the water cross section is a decreasing function of energy in the studied energy range, their values are systematically reduced and electrons lose their energy in a reduced rate, depositing more energy in higher distances, which explains the effect observed here. Significant differences have been found of about 6.6% at higher energies, demonstrating the importance of the correct

TABLE III. Material compositions: ICRU 44 and MIRD Pamphlet No. 3 tissue equivalent.

	% weight											
Element	H	C	N	O	Na	P	S	Cl	K	Ca	Fe	I
ICRU 44	10.5	12.5	2.6	73.5	0.2	0.2	0.18	0.22	0.21	0.01	0.01	0.01
MIRD Pamphlet No. 3	10.0	14.89	3.47	71.39	0.15	–	–	0.1	–	–	–	–

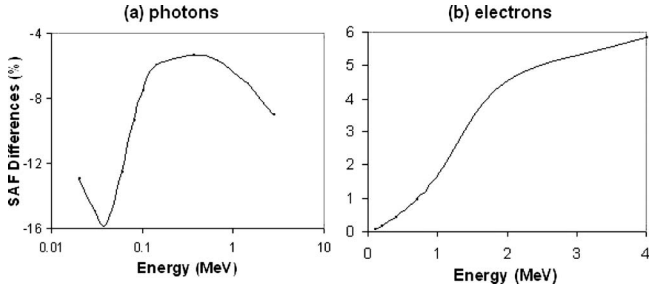

FIG. 3. Percentage differences in the SAF using different material compositions: ICRU 44 and MIRD Pamphlet no. 3 tissue equivalent for (a) photons and (b) electrons. Reference: ICRU 44.

choice of the numerical approximation in internal dosimetry calculation as already demonstrated by previous works for external beam dosimetry.

III.C. Transport parameters data in MCNP

No significant discrepancies have been detected in dose calculation in water using MCPLIB, MCPLIB02, and MCPLIB03 data. However, when comparing these results to those obtained using MCPLIB04 data, some important discrepancies have been observed. Percentage differences in the absorbed fractions in 1, 10, 100, and 1000 g water spheres for several energies from 0.01 to 2.75 MeV have been determined using MCPLIB03 and MCPLIB04 data. Figure 1 demonstrates that the discrepancies found here are consistent with the results presented by DeMarco *et al.*[19] and Ye *et al.*[32] Values obtained with MCPLIB03 are systematically lower than those obtained with MCPLIB04, the adopted reference values. The discrepancies are higher for low energies reaching their maximum value, about 9%, at 30 keV in water and decrease as the photon energy increases, becoming negligible for energies higher than 0.14 MeV.

From the comparison of the total photon cross sections obtained from MCPLIB03 and MCPLIB04 for H and O presented in Fig. 2, one can observe some differences for H in the range of 1–20 keV with maximum of about 1.5%, but even greater differences—maximum above 6%—have been found for O at the 10–30 keV energy range, which is the range where the discrepancies in dose estimates become significant. From this analysis, one can observe that the main cause for the behavior of the differences in dose is due to the differences in oxygen total cross section.

III.D. Material composition

The other aspect that should be considered carefully in any simulation is the material composition specification of the tissues. To stress this aspect, calculation results with the MIRD Pamphlet No. 3 (Ref. 4) tissue-equivalent composition and with those from ICRU 44 (Ref. 33) have been compared. Table III shows the percentage in weight of each element that makes up the tissue. Figure 3 shows the differences in specific absorbed fractions (SAFs) for photons and electrons calculated with MCNP5/MCPLIB04. They were obtained assuming that the results obtained with ICRU 44 tissue composition are the reference values. In terms of absolute values, the differences are considerable for photons reaching a maximum of 15.8% at 0.04 MeV.

The analysis at the energy of 0.04 MeV has shown that the presence of P, S, and K with 0.2%, 0.18%, and 0.21% in weight in the ICRU 44 composition, and which is not present in the tissue-equivalent composition, contributes with 6.6% difference in the result, and the presence of Ca, Fe, and I with 0.01% in weight which also is not present in the tissue-equivalent composition are responsible for other 2.2% totalizing 8.8% difference. The rest 7% difference is attributed to the differences in the % weight of H, O, N, C, Cl, and Na. The differences for electrons are substantially smaller with a trend to increase as energy increases. A maximum value of the order of 5.8% has been found at 4 MeV, the upper energy boundary in this study, with almost of all due to differences in Ca, Fe, and I% weight.

III.E. Comparison of physical models in GEANT4

The GENERAL PARTICLE SOURCE tool available in the GEANT4 distribution was employed to define the source of primary particles. The homogeneous volumetric distribution of source particles (electrons or photons) was performed by selecting the spherical shape and choosing the desired radius. Simulated sources were taken for isotropically emitted monoenergetic particles either electrons or photons.

Secondary particle production cutoff in GEANT4 is defined in terms of length units. Energy cutoffs are calculated for each material present in the simulation after particle length cutoffs are set.

The energy deposition in each sphere was scored by using the methods GetPosition( ) and GetEnergyDeposit( ) of GEANT4. For each step of all tracked particles, the step position obtained with the GetPosition( ) method was used to verify if the particle was inside or outside the sphere. Whenever the particle was inside, the energy value obtained with the GetEnergyDeposit( ) method was scored to the sphere. At the end of each event i, the total energy (E_i) and the total squared energy (E_i^2) were recorded. At the end of the run, after a number N events selected by the user, the mean energy (E_m) was calculated as the arithmetic average, and the corresponding statistical deviation was estimated from the

TABLE IV. Photon energy deposition differences in percentage, calculated with Eq. (1), obtained with different physical models: Standard (St), Penelope (Pe), and low energy. Reference: Low energy.

Sphere mass (g)	Photon energy (MeV)					
	0.01		0.1		1	
	St	Pe	St	Pe	St	Pe
1	−0.70	0.03	−1.30	0.46	−0.73	2.27
10	0.00	0.02	−1.42	0.17	0.18	0.86
100	0.00	0.00	−1.63	0.13	0.45	0.34
1000	0.00	0.00	−1.91	0.18	0.53	0.17

TABLE V. Electron energy deposition differences in percentage, calculated with Eq. (1), obtained with different physical models: Standard (St), Penelope (Pe), and low energy. Reference: Low energy.

Sphere mass (g)	Electron energy (MeV)							
	0.1		1		2		4	
	St	Pe	St	Pe	St	Pe	St	Pe
1	−0.02	−0.01	0.03	0.06	0.08	4.55	2.57	6.68
10	−0.01	−0.01	0.04	0.06	−0.11	0.05	2.15	4.73
100	−0.01	−0.01	0.05	0.06	−0.10	0.04	−0.11	0.10
1000	−0.01	−0.02	0.05	0.04	−0.09	0.04	−0.10	0.09

square root of the mean of the total squared energy minus the squared mean energy.

Energy depositions using the three physical models available in GEANT4 were compared for photons and electrons in water. The results obtained with both standard and Penelope models were compared to the low-energy model; the percentage differences are presented in Tables IV and V.

Table IV shows good agreement between the three models for energy deposition of 10 keV photons. For photons of 100 keV, the standard model predicts energy deposition which is 1%–2% less than the low-energy model for all spheres. This behavior can be explained by the differences in the total photon cross sections of both models, shown at the bottom part of Fig. 4(a). Large differences are observed for photons in the range of 5–200 keV, reaching a difference larger than 15% for energies between 20 and 30 keV. The largest differences between the Penelope and low-energy model occur for deposited energy of 1 MeV photons in the smallest sphere (2.3%). At this energy, the range of secondary electrons is on the order of the radius of the smallest sphere; therefore, differences in the stopping power of electrons are also important to be regarded. Although the largest differences between photon cross sections of Penelope and low-energy models are less than 0.7% in the energy range of this work, as shown in the middle part of Fig. 4(a), the differences between the electron stopping powers for these models are larger than 2.5% for electron energies just below 1 MeV [middle part of Fig. 4(b)].

The comparison of the deposited energy of electrons presented in Table V shows good agreement between the three models for electrons of 100 keV and 1 MeV for all spheres. For 2 MeV electrons, there is only one case of large discrepancy for the smallest sphere prediction of the Penelope model (4.6%), while for 4 MeV electrons the differences for the two smallest spheres are larger than 2% and 4.5% for standard and Penelope models, respectively. Figure 4(b) shows differences from −4% to +4% between the electron stopping power of Penelope and standard models relative to the low-energy model. Electrons of 2 and 4 MeV have ranges in water of the orders of 1 and 2 cm, respectively. Since the radii of the two smallest spheres are, respectively, 0.6 and 1.3 cm, the stopping power differences have more influence on the deposited energy values calculated for these spheres.

III.F. Absorbed fraction tables

This section presents the photon and electron AFs obtained with the two Monte Carlo codes used in this work. Five different material compositions from ICRU 44 have been considered: Water, soft tissue, lung, cortical bone, and

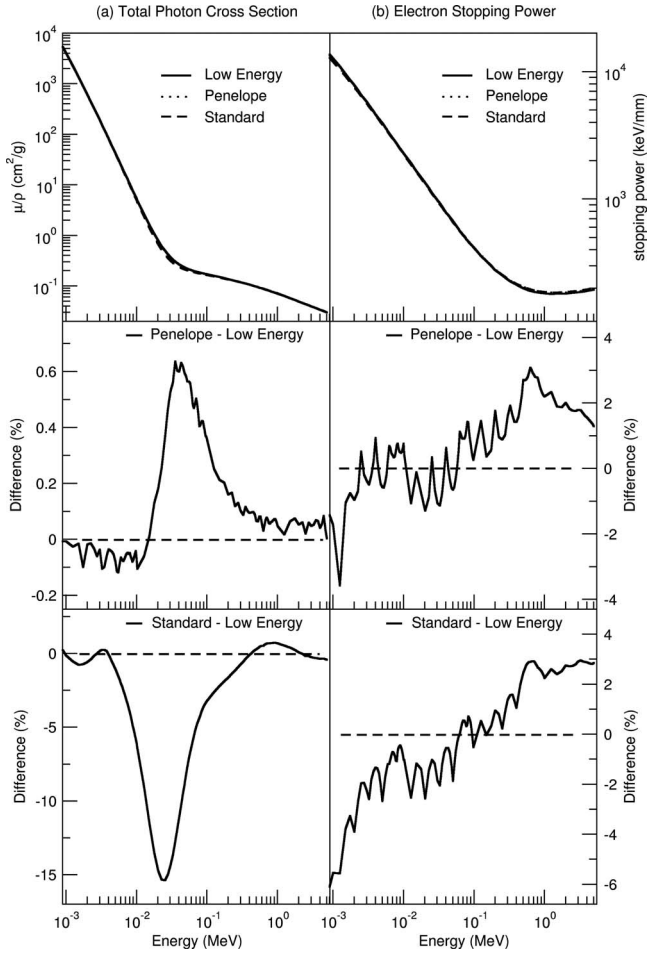

FIG. 4. (a) Total cross sections of photon interactions in water for the three electromagnetic models of GEANT4 (top)—Differences in percentage of the Penelope model (middle) and standard model (bottom) relative to the low-energy model. (b) electron stopping power in water for the three electromagnetic models of GEANT4 (top)—Differences in percentage of the Penelope model (middle) and standard model (bottom) relative to the low-energy model.

TABLE VI. Length cutoffs used in GEANT4 which correspond to energy cutoffs of 2.93 keV for photons and 9.4 keV for electrons.

	Material				
	Water	Bone	Soft tissue	Marrow	Lung
Photon	1.00 mm	0.27 mm	0.99 mm	1.20 mm	3.95 mm
Electron	7.85 μm	4.50 μm	7.50 μm	7.60 μm	30.5 μm

red bone marrow. 17 sphere sizes for photons and 19 sphere sizes for electrons have been considered. Photon and electron energy sources are those considered in the MIRD Pamphlet No. 3 and also in the work of Stabin and Konijnenberg.[9] Uniform source distribution was assumed throughout homogeneous sphere located within water.

MCNP5 calculations adopted *F8 tally for energy deposition estimator with ITS indexing mode and MCPLIB04 and EL03 cross-section libraries for photons and electrons, respectively. For the comparison of results between MCNP5 and GEANT4, the MCNP5 results were adopted as the reference values. GEANT4 calculations adopted the low-energy physical model; this choice was based on the fact that the low-energy model is the GEANT4 native package recommended for medical physics simulations. The employed energy cutoffs for photons and electrons were 2.93 and 9.4 keV, respectively. Table VI presents the length cutoffs used for photons and electrons in each material. The length cutoff in GEANT4 corresponds to a secondary particle production threshold, which is converted internally to an energy value for each material and each particle. The action of the length cutoff is to suppress the production of the particle when its mean free path is shorter than the specified cut-off value.

Absorbed fractions published by Stabin and Konijnenberg utilized unit-density spheres with tissue-equivalent composition from MIRD Pamphlet No. 3 and were evaluated as the average values between two codes: MCNP4C and EGS4. These results have been compared to the MCNP5 and GEANT4 average values obtained in the present work, considering the ICRU 44 soft tissue.

III.G. Photon absorbed fractions

Figure 5(a) shows the differences between the average values obtained here with MCNP5 and GEANT4 for soft tissue and those obtained in the work of Stabin and Konijnenberg. Basically, what can be observed from it is the same behavior observed in Fig. 1 where part of the differences is caused by the differences in the MCNP cross-section libraries mainly for low energies. Another part is due to different material compositions considered in each simulation. The maximum difference found is about 20%, corresponding to the smallest sphere at the energy of 30 keV. The other factor that should be mentioned is that the published values are limited to three digits, and in some cases, it introduced truncation errors that interfered in the estimation of the differences as can be observed particularly for the 1 g sphere and at the energy of 2.75 MeV.

Figures 5(b)–5(f) illustrate the AF relative differences between MCNP5 and GEANT4 for water, soft tissue, red bone marrow, bone, and lung tissue. It can be observed that for almost all cases the differences are around $\pm 0.5\%$ which is within the simulation uncertainties, except for higher energies, 1.46 and 2.75 MeV, where the maximum differences are, respectively, 2.2%, 2.2%, 2.3%, 1.3%, and 5.0%. For these two energies, it can also be observed that, except for bone, GEANT4 gives lower values than MCNP5. This aspect emphasizes the distinct behavior of numerical approximations and cross sections used in the different codes. Particularly for lung tissue, this aspect is accentuated in leading

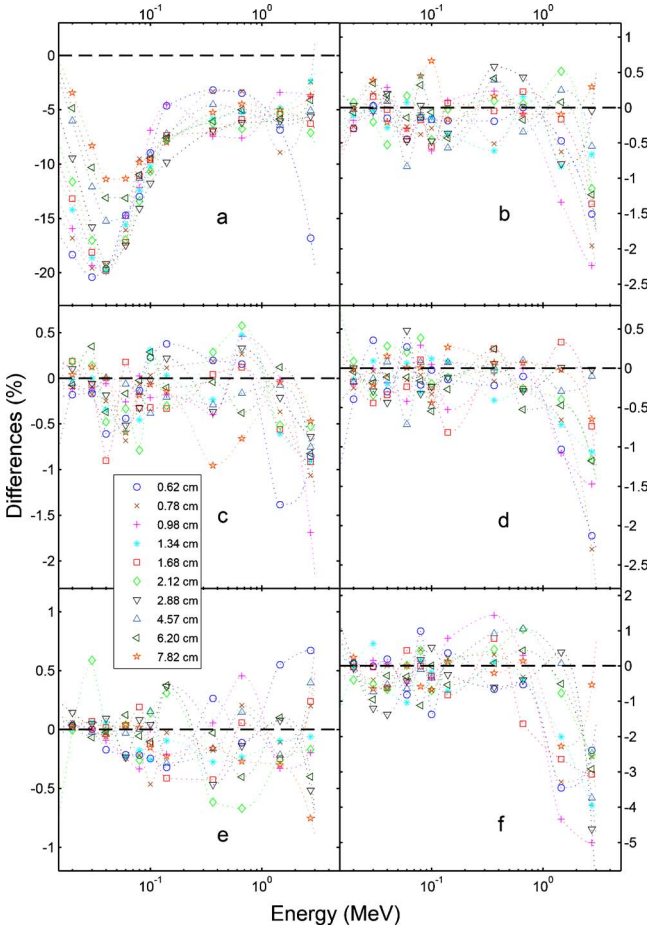

FIG. 5. Differences in AFs for several sphere sizes and photon energy sources between MCNP5/GEANT4 average values and those obtained from Stabin and Konijnenberg (a) and differences between MCNP5 and GEANT4 for (b) water, (c) soft tissue, (d) red bone marrow, (e) bone, and (f) lung. Reference: MCNP5.

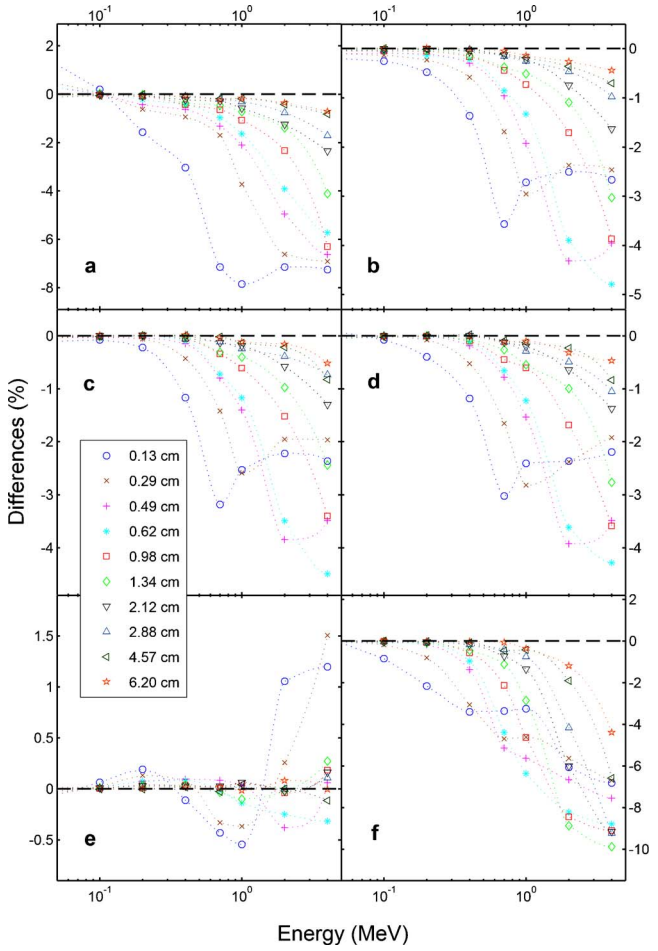

FIG. 6. Differences in AFs for several spheres sizes and electron energy sources between MCNP5/GEANT4 average values and those obtained from Stabin and Konijnenberg (a) and differences between MCNP5 and GEANT4 for (b) water, (c) soft tissue, (d) red bone marrow, (e) bone, and (f) lung. Reference: MCNP5.

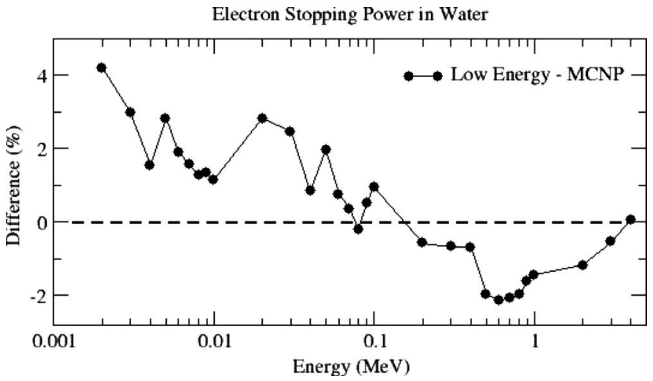

FIG. 7. Differences in stopping powers in water used in GEANT4 (low-energy model) and MCNP5.

with highly degree of heterogeneity interface—lung/water. Tables VII–XI in Appendix A show the average photon absorbed fraction values obtained from the two Monte Carlo codes for the five material compositions mentioned above.

III.H. Electron absorbed fractions

Tables XII–XVI in Appendix B show the average electron absorbed fractions from the two Monte Carlo codes and for the five material compositions. Curves in Fig. 6 show the differences in the results between the codes. Particularly, Fig. 6(a) shows the comparison of average AF values obtained here and from Ref. 9. The maximum percentage difference found is 7.8% at the energy of 1 MeV and for the smallest sphere (0.01 g). As already mentioned previously, the main causes for the differences are due to different sets of parameters of simulation, cross sections, physical models and, particularly for this case, the differences in the material composition.

Figures 6(b)–6(f) show the differences between the results of MCNP5 and GEANT4, respectively, for water, soft tissue, red bone marrow, bone, and lung tissue. Again, as already observed previously, the higher differences are located at higher energies, and particularly for lung tissue the differences are significant with maximum of about 10.0%. Three major aspects contributing to the differences can be considered here. First, observing the comparison of stopping powers in water used in both codes, one can note that for higher energies, specifically in the range of 0.2–4 MeV (see Fig. 7), the stopping powers used in MCNP are greater than those used in GEANT4. These differences increase with energy reaching its maximum at 0.6 MeV. In part, it explains why MCNP gives greater AF values than GEANT4 and why the differences increase as the energy increases in this energy range, at least for water, soft tissue, and red bone marrow which composition and densities are similar.

The second aspect is related to the peculiar behavior of each AF difference curves which we believe is related to a joint effect regarding particle's leakage connected to the volume sizes. In fact, for low energies or large volumes, the leakage of particle is very small so that the AF values is close to unity. On the other hand, for high energies or very small volumes, the leakage becomes significant so that peculiarities of physical models, algorithms, or numerical approximations in different simulations (different codes—classes I and II) also becomes relevant producing different responses in the interface.

The third aspect is related to the backscattering process which basically has to do with the differences found for bone and lungs, respectively, [Fig. 6(e) (bone sphere surrounded by water) and Fig. 6(f) (lung sphere surrounded by water)]. What we observe from these two curves is an opposite behavior. For bone/water the difference is positive (high density), while for lungs/water the difference is negative (low density). In other words, in interfaces between very different densities, the backscattering process is treated differently in both codes and this difference increases as the energy increases. In GEANT4 the contribution of the backscattered particles to energy deposition in the sphere is greater than in MCNP when the source volume has the higher density, but the opposite is true when the source volume has the lower density material.

Figure 5, in turn, shows that MCNP and GEANT provide statistically equivalent estimates for photon AF, except for 2.75 MeV photons. This can be explained by the aspects risen just before through the analysis of Fig. 6. The observed AF differences may be attributed to the increment in the number of electron tracks with energies above 0.2 MeV as just mentioned before.

IV. CONCLUSION

It becomes clear that even for simple problems as spheres and uniform radiation source as adopted in this work, the set of parameter chosen by any Monte Carlo radiation transport code simulation significantly affects the final results of the simulation. The present work covered a vast range of volume sizes and energies and one can straightly conclude from Fig. 5 that GEANT4 provides photon energy deposition estimates that are in good agreement with MCNP5 for low energies, with differences in percentage within the simulation statistical uncertainties of 0.5%, but provides relatively smaller values for higher energies. As for the electrons, the differences are larger, following the same pattern of photons, increasing for higher energies.

One can also conclude that small volumes containing high energy sources are particularly challenging problems for any Monte Carlo code, requiring careful analysis to choose the best parameters for the simulation. Certainly, this issue should be taken into account in microdosimetry applications and the correct choice of tally option in MCNP becomes more relevant for small volume targets. Even the most suitable set of parameters used for each of the codes presented significant discrepancies. The worst case is for lung tissue where absorbed fraction differences reached 5.0% and 10.0%, respectively, for photons and electrons. Problems with heterogeneous material composition where the existence of interfaces requires additional numerical approximations are expected to produce even greater discrepancies between the codes. This work also shows that small differences in weight percentage of each component of the tissue can provoke significant changes in dose estimates so that the accurate material composition data are crucial.

Another source of discrepancies comes from the different cross-section libraries used by the codes. This is an independent source of discrepancies since they originate from independent nuclear models and evaluated from different laboratories. A more detailed analysis and quantification of dose discrepancies caused by differences in cross-section data is worth to be done in the near future, taking into account different material compositions and cross-section components representing each type of interaction of photons and electrons with matter as they become more significant in the whole process of simulation and then to better estimate dose values with greater accuracy.

ACKNOWLEDGMENTS

One of the authors (C. C. Guimarães) gratefully acknowledges José Roberto Martinelli who has made this study possible, and the Brazilian agency FAPESP for financial support (Process No. 06/04188-0). Another author (F. B. Cintra) thanks the Comissão Nacional de Energia Nuclear, CNEN, for the financial support.

APPENDIX A: TABLES OF MCNP5 AND GEANT4 AVERAGE ABSORBED FRACTIONS FOR PHOTONS

Tables VII–XI in Appendix A show the average photon absorbed fraction values obtained from the two Monte Carlo codes for the five material compositions mentioned above.

TABLE VII. Average photon absorbed fractions in water.

Sphere mass (g)	Sphere radius (cm)	Energy (MeV)										
		0.02	0.03	0.04	0.06	0.08	0.1	0.14	0.364	0.662	1.46	2.75
1	0.620 351	0.2286	0.0759	0.0353	0.0162	0.0129	0.0124	0.0130	0.0148	0.0138	0.0092	0.0045
2	0.781 593	0.2776	0.0961	0.0454	0.0209	0.0165	0.0158	0.0165	0.0188	0.0178	0.0125	0.0067
4	0.984 745	0.3334	0.1212	0.0583	0.0270	0.0213	0.0203	0.0210	0.0238	0.0227	0.0166	0.0097
6	1.127 252	0.3692	0.1387	0.0674	0.0315	0.0247	0.0235	0.0242	0.0273	0.0261	0.0197	0.0120
8	1.240 701	0.3956	0.1526	0.0750	0.0351	0.0275	0.0260	0.0267	0.0302	0.0289	0.0219	0.0139
10	1.336 505	0.4165	0.1640	0.0812	0.0383	0.0300	0.0283	0.0289	0.0324	0.0313	0.0240	0.0155
20	1.683 890	0.4836	0.2049	0.1046	0.0499	0.0389	0.0365	0.0371	0.0411	0.0397	0.0314	0.0212
40	2.121 568	0.5537	0.2531	0.1338	0.0656	0.0508	0.0473	0.0476	0.0521	0.0502	0.0406	0.0286
60	2.428 589	0.5933	0.2852	0.1546	0.0769	0.0595	0.0551	0.0550	0.0597	0.0574	0.0467	0.0339
80	2.673 007	0.6206	0.3101	0.1711	0.0860	0.0666	0.0617	0.0611	0.0656	0.0633	0.0516	0.0379
100	2.879 410	0.6421	0.3300	0.1853	0.0938	0.0728	0.0671	0.0663	0.0712	0.0685	0.0559	0.0415
300	4.152 826	0.7354	0.4373	0.2675	0.1444	0.1128	0.1029	0.0995	0.1028	0.0980	0.0815	0.0626
400	4.570 776	0.7574	0.4678	0.2927	0.1610	0.1261	0.1150	0.1104	0.1133	0.1080	0.0904	0.0696
500	4.923 719	0.7731	0.4914	0.3134	0.1757	0.1375	0.1253	0.1200	0.1221	0.1164	0.0973	0.0754
600	5.232 231	0.7856	0.5111	0.3300	0.1879	0.1479	0.1346	0.1285	0.1298	0.1236	0.1029	0.0801
1000	6.203 495	0.8169	0.5652	0.3829	0.2278	0.1807	0.1638	0.1549	0.1537	0.1455	0.1223	0.0958
2000	7.815 913	0.8533	0.6357	0.4574	0.2902	0.2346	0.2133	0.1994	0.1923	0.1813	0.1527	0.1221

TABLE VIII. Average photon absorbed fractions in ICRU 44 soft tissue.

Sphere mass (g)	Sphere radius (cm)	Energy (MeV)										
		0.02	0.03	0.04	0.06	0.08	0.1	0.14	0.364	0.662	1.46	2.75
1.05	0.620 351	0.2514	0.0856	0.0424	0.0192	0.0146	0.0136	0.0138	0.0155	0.0145	0.0097	0.0048
2.1	0.781 593	0.3036	0.1081	0.0544	0.0247	0.0187	0.0174	0.0175	0.0197	0.0186	0.0132	0.0072
4.2	0.984 745	0.3623	0.1362	0.0698	0.0320	0.0241	0.0222	0.0223	0.0248	0.0238	0.0176	0.0104
6.3	1.127 252	0.3993	0.1555	0.0808	0.0372	0.0280	0.0257	0.0257	0.0285	0.0274	0.0207	0.0128
8.4	1.240 701	0.4265	0.1708	0.0894	0.0416	0.0312	0.0286	0.0284	0.0315	0.0302	0.0232	0.0146
10.5	1.336 505	0.4483	0.1834	0.0970	0.0453	0.0339	0.0311	0.0309	0.0340	0.0327	0.0252	0.0164
21	1.683 890	0.5173	0.2276	0.1239	0.0593	0.0436	0.0402	0.0395	0.0430	0.0414	0.0328	0.0224
42	2.121 568	0.5859	0.2803	0.1585	0.0775	0.0577	0.0523	0.0507	0.0545	0.0525	0.0422	0.0302
63	2.428 589	0.6247	0.3145	0.1821	0.0911	0.0677	0.0610	0.0588	0.0622	0.0601	0.0489	0.0355
84	2.673 007	0.6511	0.3402	0.2010	0.1017	0.0760	0.0681	0.0654	0.0689	0.0663	0.0541	0.0398
105	2.879 410	0.6716	0.3610	0.2170	0.1109	0.0829	0.0743	0.0712	0.0741	0.0714	0.0586	0.0434
315	4.152 826	0.7598	0.4713	0.3081	0.1697	0.1283	0.1142	0.1070	0.1072	0.1022	0.0855	0.0659
420	4.570 776	0.7798	0.5018	0.3357	0.1893	0.1438	0.1275	0.1190	0.1183	0.1128	0.0941	0.0727
525	4.923 719	0.7942	0.5255	0.3578	0.2056	0.1567	0.1395	0.1292	0.1272	0.1212	0.1017	0.0790
630	5.232 231	0.8056	0.5453	0.3759	0.2196	0.1686	0.1495	0.1388	0.1358	0.1286	0.1073	0.0843
1050	6.203 495	0.8345	0.5985	0.4302	0.2633	0.2047	0.1821	0.1672	0.1607	0.1515	0.1275	0.1001
2100	7.815 913	0.8680	0.6654	0.5073	0.3307	0.2635	0.2351	0.2149	0.2005	0.1884	0.1590	0.1267

TABLE IX. Average photon absorbed fractions in ICRU 44 red bone marrow.

Sphere mass (g)	Sphere radius (cm)	Energy (MeV)										
		0.02	0.03	0.04	0.06	0.08	0.1	0.14	0.364	0.662	1.46	2.75
1.03	0.620 351	0.2008	0.0670	0.0319	0.0155	0.0128	0.0125	0.0132	0.0151	0.0142	0.0094	0.0046
2.06	0.781 593	0.2455	0.0849	0.0410	0.0200	0.0164	0.0160	0.0168	0.0192	0.0182	0.0128	0.0069
4.12	0.984 745	0.2973	0.1075	0.0527	0.0258	0.0211	0.0205	0.0213	0.0244	0.0233	0.0171	0.0100
6.18	1.127 252	0.3309	0.1234	0.0611	0.0300	0.0245	0.0237	0.0247	0.0280	0.0268	0.0201	0.0124
8.24	1.240 701	0.3559	0.1356	0.0678	0.0335	0.0273	0.0263	0.0272	0.0308	0.0297	0.0226	0.0142
10.3	1.336 505	0.3759	0.1464	0.0736	0.0365	0.0296	0.0285	0.0295	0.0332	0.0320	0.0246	0.0159
20.6	1.683 890	0.4415	0.1831	0.0949	0.0476	0.0385	0.0367	0.0376	0.0421	0.0405	0.0322	0.0218
41.2	2.121 568	0.5111	0.2281	0.1225	0.0625	0.0502	0.0476	0.0483	0.0532	0.0513	0.0414	0.0293
61.8	2.428 589	0.5515	0.2582	0.1417	0.0731	0.0586	0.0554	0.0558	0.0611	0.0589	0.0479	0.0346
82.4	2.673 007	0.5801	0.2817	0.1567	0.0821	0.0656	0.0617	0.0622	0.0671	0.0647	0.0531	0.0387
103	2.879 410	0.6018	0.3005	0.1694	0.0898	0.0715	0.0672	0.0673	0.0725	0.0698	0.0575	0.0425
309	4.152 826	0.7016	0.4053	0.2471	0.1378	0.1108	0.1027	0.1007	0.1049	0.1004	0.0837	0.0640
412	4.570 776	0.7250	0.4343	0.2718	0.1540	0.1240	0.1146	0.1121	0.1154	0.1106	0.0922	0.0713
515	4.923 719	0.7425	0.4587	0.2917	0.1684	0.1351	0.1250	0.1215	0.1244	0.1190	0.0994	0.0768
618	5.232 231	0.7563	0.4785	0.3084	0.1802	0.1452	0.1342	0.1301	0.1317	0.1374	0.1054	0.0820
1030	6.203 495	0.7914	0.5313	0.3590	0.2186	0.1771	0.1629	0.1565	0.1564	0.1482	0.1246	0.0978
2060	7.815 913	0.8322	0.6035	0.4341	0.2800	0.2300	0.2112	0.2014	0.1956	0.1851	0.1560	0.1240

TABLE X. Average photon absorbed fractions in ICRU 44 bone.

Sphere mass (g)	Sphere radius (cm)	Energy (MeV)										
		0.02	0.03	0.04	0.06	0.08	0.1	0.14	0.364	0.662	1.46	2.75
1.92	0.620 351	0.8395	0.5688	0.3385	0.1326	0.0689	0.0459	0.0317	0.0272	0.0257	0.0194	0.0194
3.84	0.781 593	0.8720	0.6358	0.4026	0.1672	0.0887	0.0592	0.0409	0.0344	0.0327	0.0253	0.0253
7.68	0.984 745	0.8979	0.6978	0.4709	0.2095	0.1141	0.0770	0.0528	0.0436	0.0415	0.0328	0.0328
11.52	1.127 252	0.9107	0.7312	0.5124	0.2385	0.1321	0.0898	0.0615	0.0499	0.0475	0.0381	0.0381
15.36	1.240 701	0.9191	0.7534	0.5420	0.2604	0.1466	0.1003	0.0687	0.0551	0.0524	0.0423	0.0422
19.2	1.336 505	0.9248	0.7697	0.5648	0.2786	0.1589	0.1089	0.0746	0.0595	0.0564	0.0459	0.0458
38.4	1.683 890	0.9405	0.8149	0.6336	0.3411	0.2031	0.1415	0.0970	0.0753	0.0713	0.0585	0.0584
76.8	2.121 568	0.9527	0.8502	0.6973	0.4104	0.2560	0.1831	0.1270	0.0954	0.0895	0.0743	0.0742
115.2	2.428 589	0.9590	0.8711	0.7319	0.4534	0.2923	0.2119	0.1479	0.1096	0.1029	0.0852	0.0850
153.6	2.673 007	0.9628	0.8824	0.7537	0.4841	0.3198	0.2343	0.1647	0.1209	0.1130	0.0937	0.0934
192	2.879 410	0.9651	0.8912	0.7709	0.5080	0.3417	0.2534	0.1797	0.1306	0.1214	0.1013	0.1013
576	4.152 826	0.9761	0.9250	0.8396	0.6259	0.4605	0.3610	0.2663	0.1896	0.1731	0.1440	0.1430
768	4.570 776	0.9784	0.9319	0.8540	0.6543	0.4931	0.3923	0.2933	0.2085	0.1902	0.1586	0.1584
960	4.923 719	0.9799	0.9369	0.8645	0.6761	0.5185	0.4169	0.3157	0.2241	0.2035	0.1703	0.1702
1152	5.232 231	0.9811	0.9406	0.8728	0.6934	0.5389	0.4380	0.3349	0.2376	0.2158	0.1801	0.1799
1920	6.203 495	0.9841	0.9499	0.8932	0.7380	0.5953	0.4968	0.3916	0.2802	0.2518	0.2111	0.2112
3840	7.815 913	0.9874	0.9607	0.9157	0.7902	0.6675	0.5761	0.4706	0.3450	0.3091	0.2588	0.2584

TABLE XI. Average photon absorbed fractions in ICRU 44 lungs.

Sphere mass (g)	Sphere radius (cm)	Energy (MeV)										
		0.02	0.03	0.04	0.06	0.08	0.1	0.14	0.364	0.662	1.46	2.75
0.26	0.620 351	0.0696	0.0209	0.0095	0.0042	0.0033	0.0032	0.0033	0.0036	0.0028	0.0010	0.0004
0.52	0.781 593	0.0872	0.0266	0.0122	0.0054	0.0043	0.0041	0.0042	0.0046	0.0038	0.0015	0.0006
1.04	0.984 745	0.1088	0.0340	0.0157	0.0070	0.0055	0.0052	0.0054	0.0060	0.0050	0.0023	0.0009
1.56	1.127 252	0.1238	0.0391	0.0181	0.0082	0.0064	0.0061	0.0062	0.0069	0.0059	0.0029	0.0011
2.08	1.240 701	0.1352	0.0433	0.0201	0.0091	0.0071	0.0067	0.0069	0.0076	0.0066	0.0034	0.0014
2.6	1.336 505	0.1449	0.0469	0.0218	0.0098	0.0077	0.0073	0.0074	0.0082	0.0072	0.0039	0.0016
5.2	1.683 890	0.1789	0.0595	0.0281	0.0129	0.0100	0.0094	0.0095	0.0105	0.0094	0.0056	0.0025
10.4	2.121 568	0.2189	0.0754	0.0363	0.0168	0.0130	0.0121	0.0123	0.0134	0.0123	0.0079	0.0038
15.6	2.428 589	0.2456	0.0870	0.0422	0.0196	0.0151	0.0141	0.0142	0.0155	0.0143	0.0094	0.0048
20.8	2.673 007	0.2662	0.0955	0.0471	0.0220	0.0169	0.0157	0.0157	0.0170	0.0158	0.0109	0.0056
26	2.879 410	0.2829	0.1027	0.0508	0.0240	0.0184	0.0172	0.0171	0.0184	0.0171	0.0120	0.0063
78	4.152 826	0.3745	0.1487	0.0764	0.0371	0.0283	0.0261	0.0257	0.0272	0.0253	0.0188	0.0115
104	4.570 776	0.4007	0.1627	0.0848	0.0414	0.0319	0.0293	0.0287	0.0301	0.0283	0.0212	0.0131
130	4.923 719	0.4214	0.1745	0.0919	0.0451	0.0349	0.0320	0.0312	0.0324	0.0304	0.0230	0.0146
156	5.232 231	0.4386	0.1853	0.0986	0.0487	0.0374	0.0344	0.0335	0.0345	0.0325	0.0247	0.0160
260	6.203 495	0.4887	0.2165	0.1180	0.0597	0.0458	0.0420	0.0405	0.0413	0.0389	0.0301	0.0201
520	7.815 913	0.5575	0.2661	0.1499	0.0786	0.0606	0.0550	0.0528	0.0526	0.0494	0.0385	0.0274

APPENDIX B: TABLES OF MCNP5 AND GEANT4 AVERAGE ABSORBED FRACTIONS FOR ELECTRONS

Tables XII–XVI in Appendix B show the average electron absorbed fractions from the two Monte Carlo codes and for the five material compositions.

TABLE XII. Average electron absorbed fractions in water.

Sphere mass (g)	Sphere radius (cm)	Energy (MeV)						
		0.1	0.2	0.4	0.7	1	2	4
0.01	0.133 651	0.9576	0.8714	0.6504	0.3473	0.2026	0.0887	0.0434
0.1	0.287 942	0.9800	0.9395	0.8326	0.6540	0.4887	0.2043	0.0965
0.5	0.492 373	0.9881	0.9644	0.9012	0.7921	0.6815	0.3784	0.1688
1	0.620 351	0.9905	0.9713	0.9212	0.8333	0.7444	0.4753	0.2159
2	0.781 593	0.9924	0.9772	0.9374	0.8666	0.7953	0.5690	0.2797
4	0.984 745	0.9939	0.9818	0.9496	0.8940	0.8363	0.6500	0.3633
6	1.127 252	0.9947	0.9839	0.9562	0.9068	0.8562	0.6913	0.4186
8	1.240 701	0.9951	0.9853	0.9598	0.9149	0.8690	0.7175	0.4591
10	1.336 505	0.9955	0.9865	0.9625	0.9209	0.8783	0.7366	0.4888
20	1.683 890	0.9964	0.9891	0.9700	0.9369	0.9025	0.7883	0.5784
40	2.121 568	0.9972	0.9914	0.9760	0.9498	0.9224	0.8294	0.6560
60	2.428 589	0.9974	0.9924	0.9788	0.9557	0.9317	0.8504	0.6961
80	2.673 007	0.9977	0.9930	0.9808	0.9597	0.9375	0.8630	0.7214
100	2.879 410	0.9978	0.9935	0.9822	0.9622	0.9416	0.8727	0.7398
300	4.152 826	0.9984	0.9954	0.9872	0.9733	0.9590	0.9100	0.8132
400	4.570 776	0.9987	0.9957	0.9883	0.9755	0.9621	0.9172	0.8293
500	4.923 719	0.9987	0.9959	0.9892	0.9774	0.9647	0.9231	0.8402
600	5.232 231	0.9987	0.9962	0.9897	0.9788	0.9671	0.9277	0.8493
1000	6.203 495	0.9989	0.9969	0.9912	0.9817	0.9715	0.9376	0.8712

TABLE XIII. Average electron absorbed fractions in ICRU 44 soft tissue.

Sphere mass (g)	Sphere radius (cm)	Energy (MeV)						
		0.1	0.2	0.4	0.7	1	2	4
0.01	0.133 651	0.9601	0.8777	0.6642	0.3652	0.2128	0.0926	0.0453
0.11	0.287 942	0.9814	0.9428	0.8399	0.6674	0.5060	0.2142	0.1010
0.53	0.492 373	0.9888	0.9662	0.9057	0.8006	0.6947	0.3957	0.1767
1.05	0.620 351	0.9912	0.9732	0.9249	0.8401	0.7544	0.4924	0.2260
2.1	0.781 593	0.9929	0.9785	0.9403	0.8727	0.8042	0.5839	0.2932
4.2	0.984 745	0.9943	0.9828	0.9522	0.8986	0.8430	0.6625	0.3800
6.3	1.127 252	0.9951	0.9849	0.9580	0.9108	0.8624	0.7028	0.4362
8.4	1.240 701	0.9954	0.9862	0.9616	0.9187	0.8746	0.7285	0.4758
10.5	1.336 505	0.9958	0.9872	0.9646	0.9242	0.8834	0.7464	0.5058
21	1.683 890	0.9966	0.9896	0.9713	0.9399	0.9067	0.7958	0.5935
42	2.121 568	0.9973	0.9918	0.9772	0.9518	0.9254	0.8365	0.6688
63	2.428 589	0.9976	0.9927	0.9801	0.9574	0.9344	0.8559	0.7070
84	2.673 007	0.9978	0.9934	0.9816	0.9612	0.9399	0.8689	0.7318
105	2.879 410	0.9980	0.9938	0.9827	0.9639	0.9439	0.8777	0.7499
315	4.152 826	0.9986	0.9956	0.9878	0.9745	0.9607	0.9132	0.8203
420	4.570 776	0.9986	0.9960	0.9890	0.9769	0.9638	0.9209	0.8348
525	4.923 719	0.9988	0.9963	0.9898	0.9781	0.9666	0.9258	0.8467
630	5.232 231	0.9988	0.9964	0.9902	0.9794	0.9680	0.9295	0.8554
1050	6.203 495	0.9990	0.9970	0.9918	0.9825	0.9726	0.9405	0.8753

TABLE XIV. Average electron absorbed fractions in ICRU 44 red bone marrow.

Sphere		Energy (MeV)						
Mass (g)	Radius (cm)	0.1	0.2	0.4	0.7	1	2	4
0.01	0.133 651	0.9593	0.8745	0.6575	0.3557	0.2075	0.0909	0.0446
0.10	0.287 942	0.9811	0.9417	0.8363	0.6598	0.4959	0.2088	0.0993
0.52	0.492 373	0.9887	0.9657	0.9037	0.7965	0.6878	0.3858	0.1734
1.03	0.620 351	0.9910	0.9726	0.9234	0.8372	0.7490	0.4826	0.2215
2.06	0.781 593	0.9928	0.9780	0.9389	0.8699	0.7994	0.5756	0.2865
4.12	0.984 745	0.9943	0.9825	0.9511	0.8960	0.8398	0.6551	0.3710
6.18	1.127 252	0.9949	0.9847	0.9572	0.9091	0.8592	0.6960	0.4264
8.24	1.240 701	0.9954	0.9860	0.9610	0.9172	0.8720	0.7217	0.4670
10.3	1.336 505	0.9957	0.9870	0.9637	0.9230	0.8803	0.7412	0.4965
20.6	1.683 890	0.9966	0.9895	0.9710	0.9388	0.9049	0.7918	0.5856
41.2	2.121 568	0.9972	0.9915	0.9769	0.9510	0.9240	0.8330	0.6624
61.8	2.428 589	0.9975	0.9926	0.9796	0.9568	0.9327	0.8527	0.7009
82.4	2.673 007	0.9978	0.9931	0.9813	0.9607	0.9391	0.8649	0.7262
103	2.879 410	0.9979	0.9937	0.9828	0.9633	0.9427	0.8750	0.7442
309	4.152 826	0.9986	0.9957	0.9875	0.9744	0.9597	0.9119	0.8175
412	4.570 776	0.9985	0.9960	0.9889	0.9762	0.9632	0.9195	0.8323
515	4.923 719	0.9986	0.9961	0.9895	0.9777	0.9656	0.9243	0.8437
618	5.232 231	0.9988	0.9964	0.9901	0.9790	0.9673	0.9284	0.8524
1030	6.203 495	0.9989	0.9969	0.9915	0.9818	0.9723	0.9388	0.8739

TABLE XV. Average electron absorbed fractions in ICRU 44 bone.

Sphere mass (g)	Sphere radius (cm)	Energy (MeV)						
		0.1	0.2	0.4	0.7	1	2	4
0.02	0.133 651	0.9766	0.9280	0.7988	0.5898	0.4102	0.1631	0.0778
0.19	0.287 942	0.9889	0.9663	0.9055	0.7994	0.6941	0.4015	0.1768
0.96	0.492 373	0.9934	0.9800	0.9442	0.8818	0.8170	0.6111	0.3227
1.92	0.620 351	0.9948	0.9840	0.9554	0.9051	0.8527	0.6841	0.4135
3.84	0.781 593	0.9958	0.9871	0.9642	0.9244	0.8822	0.7447	0.5080
7.68	0.984 745	0.9966	0.9897	0.9712	0.9392	0.9059	0.7942	0.5936
11.52	1.127 252	0.9971	0.9909	0.9749	0.9464	0.9168	0.8187	0.6390
15.36	1.240 701	0.9974	0.9917	0.9769	0.9511	0.9239	0.8343	0.6677
19.2	1.336 505	0.9975	0.9923	0.9785	0.9543	0.9290	0.8453	0.6886
38.4	1.683 890	0.9980	0.9938	0.9827	0.9633	0.9431	0.8754	0.7456
76.8	2.121 568	0.9984	0.9950	0.9860	0.9705	0.9545	0.8990	0.7935
115.2	2.428 589	0.9986	0.9956	0.9877	0.9741	0.9596	0.9109	0.8166
153.6	2.673 007	0.9987	0.9959	0.9887	0.9758	0.9630	0.9181	0.8319
192	2.879 410	0.9988	0.9962	0.9895	0.9778	0.9655	0.9236	0.8424
576	4.152 826	0.9992	0.9973	0.8724	0.9841	0.9754	0.9453	0.8851
768	4.570 776	0.9992	0.9975	0.9931	0.9855	0.9775	0.9496	0.8939
960	4.923 719	0.9992	0.9977	0.9936	0.9865	0.9787	0.9530	0.9008
1152	5.232 231	0.9993	0.9979	0.9939	0.9876	0.9800	0.9549	0.9068
1920	6.203 495	0.9995	0.9981	0.9949	0.9892	0.9827	0.9620	0.9189

TABLE XVI. Average electron absorbed fractions in ICRU 44 lungs.

Sphere mass (g)	Sphere radius (cm)	Energy (MeV)						
		0.1	0.2	0.4	0.7	1	2	4
0.003	0.133 651	0.8412	0.5452	0.1740	0.0740	0.0472	0.0221	0.0110
0.026	0.287 942	0.9260	0.7762	0.4344	0.1797	0.1103	0.0493	0.0243
0.13	0.492 373	0.9566	0.8679	0.6423	0.3413	0.2039	0.0872	0.0422
0.26	0.620 351	0.9652	0.8946	0.7114	0.4381	0.2668	0.1115	0.0533
0.52	0.781 593	0.9724	0.9159	0.7683	0.5345	0.3502	0.1437	0.0678
1.04	0.984 745	0.9781	0.9329	0.8142	0.6203	0.4480	0.1863	0.0864
1.56	1.127 252	0.9809	0.9412	0.8370	0.6650	0.5044	0.2168	0.0997
2.08	1.240 701	0.9824	0.9468	0.8512	0.6936	0.5439	0.2420	0.1105
2.6	1.336 505	0.9837	0.9501	0.8614	0.7144	0.5718	0.2627	0.1192
5.2	1.683 890	0.9870	0.9605	0.8896	0.7700	0.6513	0.3432	0.1533
10.4	2.121 568	0.9894	0.9683	0.9119	0.8155	0.7193	0.4388	0.1973
15.6	2.428 589	0.9910	0.9722	0.9226	0.8384	0.7523	0.4947	0.2287
20.8	2.673 007	0.9918	0.9745	0.9298	0.8516	0.7750	0.5339	0.2544
26	2.879 410	0.9922	0.9764	0.9345	0.8630	0.7904	0.5616	0.2761
78	4.152 826	0.9946	0.9835	0.9540	0.9036	0.8517	0.6849	0.4131
104	4.570 776	0.9952	0.9850	0.9583	0.9112	0.8654	0.7117	0.4517
130	4.923 719	0.9952	0.9861	0.9613	0.9177	0.8742	0.7308	0.4824
156	5.232 231	0.9956	0.9867	0.9632	0.9228	0.8819	0.7450	0.5068
260	6.203 495	0.9964	0.9888	0.9691	0.9351	0.8992	0.7837	0.5721

[a]Author to whom correspondence should be addressed. Electronic mail: hyoriyaz@ipen.br; Also at Instituto de Pesquisas Energéticas e Nucleares, Ipen-Cnen/SP, Centro de Engenharia Nuclear (CEN), Cidade Universitária, Caixa Postal 11049, 05422-270 Pinheiros, São Paulo, Brazil; Telephone: +55 (11) 3133-9482; Fax: +55 (11)3133-9423.

[1]W. van der Zee, A. Hogenbirk, and S. C. van der Marck, "ORANGE: A Monte Carlo dose engine for radiotherapy," Phys. Med. Biol. **50**, 625–641 (2005).
[2]R. Loevinger and A. A. Berman, "A revised schema for calculating the absorbed dose from biologically distributed radionuclides," MIRD Pamphlet No. 1, revised ed. (The Society of Nuclear Medicine, New York, 1976).
[3]M. Berger, "MIRD Pamphlet No. 2: Energy deposition in water by photons from point isotropic sources," J. Nucl. Med. **9**, 15–25 (1968).
[4]G. Brownell, W. Ellett, and R. Reddy, "Absorbed fractions for photon dosimetry," MIRD Pamphlet No. 3 (The Society of Nuclear Medicine, New York, 1968).
[5]G. Akabani, J. W. Poston, and W. E. Bolch, "Estimates of beta absorbed fractions in small tissue volumes for selected radionuclides," J. Nucl. Med. **32**, 835–839 (1991).
[6]W. R. Nelson, H. Hirayama, and D. W. O. Rogers, "The EGS4 code system," SLAC Report No. 265 (Stanford University, Stanford, CA, 1985).
[7]W. Snyder, M. Ford, and G. Warner, "Estimates of specific absorbed fractions for photon sources uniformly distributed in various organs of a heterogeneous phantom," MIRD Pamphlet No. 5, revised ed. (The Society of Nuclear Medicine, New York, 1978).
[8]J. A. Siegel and M. G. Stabin, "Absorbed fractions for electrons and beta particles in spheres of various sizes," J. Nucl. Med. **35**, 52–56 (1994).
[9]M. G. Stabin and M. W. Konijnenberg, "Re-evaluation of absorbed fractions for photons and electrons in spheres of various sizes," J. Nucl. Med. **41**, 149–160 (2000).
[10]J. F. Briesmeister, "MCNP—A general Monte Carlo N-particle transport code, version 4B," Los Alamos National Laboratory Report No. LA-12625-M, 1997.
[11]J. F. Briesmeister, "MCNP: A general Monte Carlo N-particle transport code, version 4C," Los Alamos National Laboratory Report No. LA-13709-M, 2000.
[12]X-5 Monte Carlo Team, "MCNP: A general Monte Carlo N-particle transport code, version 5," Los Alamos National Laboratory Report No.LA-UR-03-1987, 2003.
[13]S. Agostinelli *et al.*, "GEANT4—A simulation toolkit," Nucl. Instrum. Methods Phys. Res. A **506**, 250–303 (2003).
[14]J. H. Hubbell, W. J. Veigele, E. A. Briggs, R. T. Brown, D. T. Cromer, and J. R. Howerton, "Atomic form factors, incoherent scattering functions, and photon scattering cross sections," J. Phys. Chem. Ref. Data **4**, 471–538 (1975).
[15]M. J. Berger, "Monte Carlo calculations of the penetration and diffusion of fast charged particles," in *Methods in Computational Physics*, edited by B. Alder, S. Fernbach, and M. Rotenberg (Academic, New York, 1993), Vol. 1.
[16]P. A. Love, D. G. Lewis, I. A. M. Al-Affan, and C. W. de Smith, "Comparison of EGS4 and MCNP Monte Carlo codes when calculating radiotherapy depth doses," Phys. Med. Biol. **43**, 1351–1357 (1998).
[17]R. Jeraj, P. J. Keall, and P. M. Ostwald, "Comparison between MCNP, EGS4 and experiment for clinical electron beams," Phys. Med. Biol. **44**, 705–717 (1999).
[18]D. R. Schaart, J. T. Jansen, J. Zoetelief, and P. F. de Leege, "A comparison of MCNP4C electron transport with ITS 3.0 and experiment at incident energies between 100 keV and 20 MeV: Influence of voxel size, substeps and energy indexing algorithm," Phys. Med. Biol. **47**, 1459–1484 (2002).
[19]J. J. DeMarco, R. E. Wallace, and K. Boedeker, "An analysis of MCNP cross-sections and tally methods for low-energy photon emitters," Phys. Med. Biol. **47**, 1321–1332 (2002).
[20]N. Reynaert, H. Palmans, H. Thierens, and R. Jeraj, "Parameter dependence of the MCNP electron transport in determining dose distributions," Med. Phys. **29**, 2446–2454 (2002).
[21]N. F. Mourtada, C. G. Soares, S. M. Seltzer, P. M. Bergstrom, Jr., J. M. Fernández-Varea, J. Asenjo, and S. H. Lott, "Dosimetry characterization of a ^{32}P source wire used for intravascular brachytherapy with automated stepping," Med. Phys. **30**, 959–971 (2003).
[22]N. Jabbari, B. Hashemi-Malayeri, A. R. Farajollahi, A. Kazemnejad, A. Shafaei, and S. Jabbari, "Comparison of MCNP4C and EGSnrc Monte Carlo codes in depth-dose calculation of low energy clinical electron beams," J. Phys. D: Appl. Phys. **40**, 4519–4524 (2007).
[23]H. W. Lewis, "Multiple scattering in an infinite medium," Phys. Rev. **78**, 526–529 (1950).

[24]M. C. White, "Photoatomic data library MCPLIB04: A new photoatomic library based on data from ENDF/B-VI release 8," Los Alamos National Laboratory Internal Memorandum No. X-5:MCW-02-111, 2002.
[25]D. E. Cullen, J. H. Hubbel, and L. D. Kissel, "EPDL97: The evaluated photon data library, '97 Version," Lawrence Livermore National Laboratory Report No. UCRL-50400, 1997.
[26]K. Amako *et al.*, "Comparison of Geant4 electromagnetic physics models against the NIST reference data," IEEE Trans. Nucl. Sci. **52**, 910–918 (2005).
[27]N. E. Poon and F. Verhaegen, "Accuracy of the photon and electron physics in Geant4 for radiotherapy applications," Med. Phys. **32**, 1696–1711 (2005).
[28]O. Kadri, V. N. Ivanchenko, F. Gharbi, and A. Trabelsi, "GEANT4 simulation of electron energy deposition in extended media," Nucl. Instrum. Methods Phys. Res. B **258**, 381–387 (2007).
[29]S. T. Perkins, D. E. Cullen, and S. M. Seltzer, "Tables and graphs of electron-interaction cross-sections from 10 eV to 100 GeV derived from the LLNL evaluated electron data library EEDL," Lawrence Livermore Laboratory Report No. UCRL-50400, 1997.
[30]S. T. Perkins, D. E. Cullen, M. H. Chen, J. H. Hubbell, J. Rathkopf, and J. Scofield, "Tables and graphs of atomic subshells and relaxation data derived from the LLNL evaluated atomic data library EADL, Z=1–100," Lawrence Livermore Laboratory Report No. UCRL-50400, 1997.
[31]F. Salvat, J. M. Fernández-Varea, E. Acosta, and J. Sempau, "PENELOPE: A code system for Monte Carlo simulation of electron and photon transport," Workshop Proceedings, OECD Nuclear Energy Agency, Issy-les-Moulineaux, 2001.
[32]S. J. Ye, I. A. Brezovich, P. Pareek, and S. A. Naqvi, "Benchmark of PENELOPE code for low-energy photon transport: Dose comparisons with MCNP4 and EGS4," Phys. Med. Biol. **49**, 387–397 (2004).
[33]ICRU Report No. 44, "Tissue substitutes in radiation dosimetry and measurement" (International Commission on Radiation Units and Measurements, Bethesda, MD, 1989).